学位論文

Involvement of ferroptosis-defensive xCT/GPX4 axis in radioresistance and its impacts on prognosis in oral squamous cell carcinoma
（口腔扁平上皮癌の放射線抵抗性におけるフェロトーシス防御性 xCT/GPX4 axis の関与と予後への影響）

石川　紘平

Kohei　Ishikawa

熊本大学大学院医学教育部博士課程医学専攻歯科口腔外科学

指導教員

中山　秀樹　教授

熊本大学大学院医学教育部博士課程医学専攻歯科口腔外科学

2024 年 3 月

学　位　論　文

論 文 題 名　：　**Involvement of ferroptosis-defensive xCT/GPX4 axis in radioresistance and its impacts on prognosis in oral squamous cell carcinoma**

（口腔扁平上皮癌の放射線抵抗性における
フェロトーシス防御性 xCT/GPX4 axis の関与と予後への影響）

著 者 名 ：　石　川　紘　平
Kohei Ishikawa

指導教員名 ：熊本大学大学院医学教育部博士課程医学専攻歯科口腔外科学
中　山　秀　樹　教授

審査委員名　：耳鼻咽喉科・頭頸部外科学担当教授　折　田　頼　尚
放射線治療医学担当教授　大　屋　夏　生
微生物学担当教授　澤　智　裕
消化器外科学担当特任准教授　馬　場　祥　史

2024年3月

Title: Involvement of ferroptosis-defensive xCT/GPX4 axis in radioresistance and its impacts on prognosis in oral squamous cell carcinoma

Abstract

Aim: Radiotherapy, the mainstay treatment for patients with advanced oral squamous cell carcinoma (OSCC), has low clinical efficacy, resulting in poor prognosis. Radiation induces ferroptosis, a form of cell death driven by iron-dependent lipid peroxidation. Since the xCT/glutathione peroxidase 4 (GPX4) axis is predominantly involved in the ferroptosis defense system, targeting this axis may potentiate cancer cell vulnerability to ferroptosis.

Methods: We examined the expression of xCT and GPX4 in the tumor cells of biopsy specimens using immunohistochemistry and evaluated the radiation-mediated antitumor effects of the ferroptosis inducers, erastin and RSL3, that act by inhibiting xCT and GPX4, respectively.

Results: Univariate analysis revealed that high immunohistochemical expression of xCT was correlated with shorter survival, and high GPX4 expression was an independent poor prognostic factor, indicating that the xCT/GPX4 axis influences the clinical outcome of OSCC. Analyses using two types of OSCC cell lines revealed that the clonogenic survival

of irradiated cells was increased by the ferroptosis inhibitor ferrostatin-1, and decreased by erastin and RSL3. The enhanced antitumor effects of erastin and RSL3 were accompanied by increased lipid peroxidation, which was suppressed by the iron chelator deferoxamine. Erastin and RSL3 enhance the effects of radiation on OSCC cells in a mouse xenograft model; these effects were associated with increased expression of the lipid peroxidation marker 4-hydroxynonenal in tumor cells.

Conclusions: xCT/GPX4 axis is involved in the tumor resistance against radiation through the inhibition of ferroptosis in OSCC. Furthermore, radiotherapy combined with ferroptosis induction by targeting the xCT/GPX4 axis may improve patient prognosis in advanced OSCC.

Keywords: xCT, GPX4, ferroptosis, radiotherapy, head and neck squamous cell carcinoma

Introduction

Although radiotherapy has long been the mainstay of treatment in patients with locally advanced head and neck squamous cell carcinoma (HNSCC), including oral squamous cell carcinoma (OSCC), its clinical efficacy remains low, resulting in poor prognosis.[1, 2] This dismal outcome is mainly attributable to the development of radioresistant defense mechanisms in cancer cells to evade radiation-induced cell death.[2-4] Thus, identifying a strategy to overcome such mechanisms and improve the patient prognosis is challenging.

Ferroptosis, a novel type of regulated cell death driven by iron-dependent lipid peroxidation, has recently been found to be induced by radiation and implicated in the antitumor effects of radiation.[5-7] Radiation is mechanistically presumed to provoke lipid peroxidation by inducing excessive reactive oxygen species (ROS) production,[8, 9] and ACSL4 expression, which promotes the biosynthesis of polyunsaturated fatty acids containing phospholipids that are particularly susceptible to peroxidation.[10-12] Therefore, suppression of the ferroptosis defense system, which can detoxify lipid peroxides to a non-toxic level, may enhance the effect of radiotherapy against OSCC.

The xCT/glutathione peroxidase 4 (GPX4) axis is believed to predominantly constitute the ferroptosis defense system.[13, 14] xCT (also known as SLC7A11) is a core component of the cystine/glutamate antiporter system x^-_c, and plays an essential role in

glutathione biosynthesis via cystine uptake and antioxidant defense.[14-16] GPX4 is a pivotal inhibitor of ferroptosis and prevents ferroptosis by utilizing glutathione to reduce phospholipid (PL) hydroperoxides to nontoxic PL alcohols.[16-18]

Collectively, the xCT/GPX4 axis may be a key determinant of the antitumor effects of radiotherapy. However, no studies have investigated the role of the xCT/GPX4 axis in OSCC and its potential as a therapeutic target. Accordingly, to determine the clinical implications of the xCT/GPX4 axis in OSCC, we first examined the expression status of xCT and GPX4 in OSCC biopsy specimens using immunohistochemical analysis and then evaluated the radiation-mediated antitumor effects of two types of ferroptosis inducers, erastin and RSL3, that act by inhibiting xCT and GPX4, respectively, through *in vitro* and *in vivo* analyses.

Materials and Methods

Reagents

Erastin, ferroptosis inhibitor ferrostatin-1,[19] and deferoxamine (DFO) were purchased from Sigma-Aldrich (St. Louis, MO, USA), and RSL3 was purchased from Selleckchem (Houston, TX, USA).

Cell lines and cell culture

A human OSCC cell line, HSC-2 was obtained from the Japanese Collection of Research Bioresources (JCRB) bank of the National Institutes of Biomedical Innovation, Health and Nutrition (Osaka, Japan). The human OSCC cell line HOC313 was donated by XXX university. All cell lines were cultured in DMEM supplemented with 10% fetal bovine serum (FBS) and maintained under humidified 5% CO_2 incubation at 37°C.

Irradiation

A single 6 Gy dose of X-ray irradiation was administered in a 150-KVp X-ray generator (Model MBR-1520R, Hitachi, Tokyo, Japan) with a total filtration of 0.5 mm aluminum plus 0.1 mm copper filter. The dose rate measured using a thimble ionization chamber (IC 17A; Far West Technology, Goleta, CA, USA) was 1.01 Gy/min.

Clonogenic assay

Cells (2.0×10^5) per well were incubated in DMEM with 10% FBS overnight. The cells were then treated with 2.5 μM erastin, 1 μM RSL3, and 5 μM ferrostatin-1 for 24 h, followed by a single 6 Gy dose of X-ray irradiation. After irradiation, the cells (1×10^4) were transferred to a gelatin-coated 60 mm culture dish (Asahi Techno Glass Co., LTD,

Shizuoka, Japan) and cultured in DMEM with 10% FBS. After 10 days, the cells were fixed with 99.5% methanol and stained with Giemsa solution (Wako, Osaka, Japan).

Lipid peroxide measurement

To evaluate lipid peroxides, cells were plated on 35-mm glass-bottom dishes and incubated in DMEM with 10% FBS overnight. The medium was treated with 2.5 μM erastin, 1 μM RSL3, and 5 μM ferrostatin-1, followed by a single 6 Gy dose of X-ray irradiation. After 24 h, the cells were exposed to Liperfluo (Dojindo Laboratories, LTD, Kumamoto, Japan) for 30 min at 37°C in the dark for lipid peroxide detection, followed by observation under a fluorescence microscope (BZ-7000, Keyence, Osaka, Japan). All images are representative of three independent experiments. Liperfluo fluorescence intensity was analyzed by measuring at least 200 cells for each treatment condition. Fluorescence intensity was measured using the ImageJ software (National Institutes of Health, Bethesda, MD, USA).

Reactive oxygen species (ROS) measurement

Dichlorodihydrofluorescein diacetate (DCFH-DA) was used to evaluate ROS production. OSCC cells were seeded in 96-well culture plates (n=8) at 8,000 cells/well and incubated

in DMEM supplemented with 10% FBS for 24 h. After changing the medium to the indicated conditions, a single 6 Gy dose of X-ray irradiation was administered. After an additional 24 h of incubation, the medium was incubated with the DCFH-DA solution (ROS Assay Kit-Highly Sensitive DCFH-DA; Dojindo Laboratories, Ltd.) for 0.5 h. The DCFH-DA solution was then replaced with Hank's balanced salt solution (HBSS) and the fluorescence intensity was measured at Ex/Em =485 nm/510 nm using a multi-grating microplate reader. SH-9000Lab (CORONA Electric Co. Ltd., Ibaraki, Japan). The fluorescence intensity was visualized using a microscope (BZ-7000, Keyence).

Tumor transplantation

All animals were housed under a 12-h dark-light cycle (light from 07:00 to 19:00) at 22 ± 1°C with ad libitum food and water. The Animal Care and Use Committee of XXX approved the protocols for the animal experiments. Female BALB/c nude mice (5 weeks old, 16–20 g) were purchased from Jackson Laboratory (Bar Harbor, ME, USA). HSC-2 cells (1.0×10^7 cells/100 μL of phosphate-buffered saline) were inoculated subcutaneously into the right dorsal flank under anesthesia induced with 2% isoflurane. Tumor size was measured using calipers every other day starting from 10 days after cell inoculation and calculated as V (mm^3) = $(L \times W^2)/2$, where L and W are the length and

width of the tumor, respectively.

Drug administration and irradiation schedule in the mouse model

When the tumor size reached approximately 100 mm^3, the mice were randomized into four groups (three animals per group): 1) control, 2) erastin alone, 3) radiation alone, and 4) erastin and radiation combination. Erastin (15 mg/kg body weight, dissolved in 5% DMSO + 95% corn oil) was prepared according to a previous study by Shibata et al.[20] and injected intraperitoneally. Cell-implanted mice were administered erastin at a dose of 15 mg/kg/day at 24-h intervals for 10 days. During radiotherapy, the anesthetized mice were locally irradiated with 3 Gy X-rays for 10 days. For RSL3, the mice were similarly divided into four groups (three animals per group): 1) control, 2) RSL3 alone, 3) radiation alone, and 4) RSL3 and radiation combination. RSL3 (5 mg/kg body weight, dissolved in 2% DMSO + 30% PEG300 + 2% Tween 80 + H_2O) was adjusted according to a previous study by Cui et al.[21] and injected intraperitoneally. Cell-implanted mice were administered RSL3 at 24-h intervals for 10 days at a dose of 5 mg/kg/day. For radiotherapy, anesthetized mice were locally irradiated with a single 3 Gy dose of X-ray/day for 10 days.

Clinical samples from the patients and the evaluation of therapeutic effects

For pathological analysis, primary oral cancer tissue samples were obtained from 92 patients with advanced OSCC who were treated at our University Hospital between 2004 and 2014. All patients were treated preoperatively with concurrent chemoradiotherapy with a total dose of 30 Gy, followed by radical surgery in a phase II study.[22-24] Radiotherapy was administered at a daily dose of 2 Gy, 5 times a week for 15 days. For pathological evaluation of the therapeutic effects, the pathological response of the primary tumors was graded according to the criteria proposed by Shimosato et al.[25] The grading was as follows: grade I, tumor structures are not destroyed; grade IIa, the destruction of the tumor structure is mild (i.e., viable tumor cells are frequently observed); grade IIb, the destruction of the tumor structure is severe (i.e., viable tumor cells are present in small areas); grade III, nonviable tumor cells are present, and grade IV, no tumor cells remain. Furthermore, based on the presence or absence of viable tumor cells, we classified the pathological response to chemoradiotherapy into two groups (grade I, II, and IIb; and grade III and IV). This study complied with the guidelines of our University Ethics Committee. The nature and purpose of the study were explained to all patients, and their informed consent was obtained.

Immunohistochemistry

Formalin-fixed specimens were embedded in paraffin, cut into 4 μm sections, and mounted on MAS-GP-coated slides (Matunami Glass Ind., LTD, Osaka, Japan). After deparaffinization and rehydration, the sections were heated in an autoclave in 10 μmol/L citrate buffer (pH 6.0) for 15 min at 121 °C for antigen retrieval. The sections were then incubated with 3% H_2O_2 in absolute methanol for 30 min to block endogenous peroxidase activity. Then, nonspecific background staining was blocked using Protein Block Serum Free Reagent (Dako, Glostrup, Denmark) for 15 min, followed by overnight incubation at 4°C with anti-GPX4 (1:100 dilution, ab125066, Abcam, Cambridge, UK), anti- xCT (1:400 dilution, ab37185, Abcam), anti- Ki-67(1: 100 dilution, M7240, Dako), and anti-4-hydroxynonenal (4-HNE) (1:250 dilution, ab46545, Abcam) antibodies diluted in phosphate-buffered saline containing 1% bovine serum albumin. This was followed by sequential 60 min incubations with secondary antibodies (EnVision+ System-HRP Labelled Polymer; Dako) and visualization with the Liquid DAB+ Substrate Chromogen System (Dako). All slides were lightly counterstained with hematoxylin eosin for 30 s before dehydration and mounting.

Evaluation of the immunohistochemical staining results

For Ki-67 and 4-HNE evaluation of mouse tumors, we counted positive tumor cells in each of the five high-power fields (×20 objective and ×10 ocular) in three sections from each group. The expression of xCT and GPX4 was evaluated as the percentage of positive tumor cells in the high-power fields (×20 objective and ×10 ocular). Staining intensity was scored as follows: 0 (no reaction), 1 (weakly positive), 2 (positive), and 3 (strongly positive). The positivity rate of stained tumor cells was scored in three stages: 1 (< 10%), 2 (10–50%), and 3 (> 51%). The score was the sum of the staining intensity and positivity rate, and the tumors were classified into two groups: a high expression group (total score of 3 or more) and low expression group (total score of 2 or less). Two independent observers (KI and YM) who were blinded to the immunohistochemical results interpreted the data. Immunohistochemical staining scores that were inconsistent between the two examiners were determined by consensus.

Multiplex immunohistochemistry (IHC)

Multiplex IHC was performed using the Opal^{TM} 4-Color Manual IHC Kit (AKOYA, NEL810001KT) according to the manufacturer's instructions. Briefly, samples were microwaved in AR buffer for epitope retrieval and microwave treatment. Blocking was performed by incubating the samples in blocking buffer for 10 min at room temperature

(RT). The samples were then incubated with the primary antibodies anti-GPX4 (1:100 dilution, ab125066, Abcam), xCT (1:400 dilution, ab37185, Abcam), and anti-4-HNE (1:250 dilution, ab46545, Abcam) for 24 h at RT. Next, incubation with the Polymer HRP Ms+Rb was performed for 10 min at RT. Opal signals were generated by incubating the samples with the Opal Fluorophore Working Solution containing the Opal 520, Opal 570, and Opal 690 fluorophores for 10 min at RT. The microwave treatment was performed for stripping the primary-secondary-HRP complex to allow the introduction of the next primary antibody. To detect the next target, the protocol was resumed during the blocking step. Finally, the samples were incubated with DAPI Working Solution for counterstaining for 5 min at RT and mounted with the VECTASHIELD Hard Set (Vector Laboratories, Burlingame, USA). The optical signals were visualized using a microscope (BZ-7000, Keyence).

Statistical analysis

The expression levels of xCT and GPX4 in OSCC tissues and their relationships with the clinicopathological parameters were analyzed using the chi-square test. The Cox proportional hazards regression model was used for multivariate survival analysis. Overall survival (OS) was defined as the time from the start of treatment to death from

any cause, while disease-free survival (DFS) was defined as the time from the start of treatment to death from any cause, recurrence of oral cancer, or occurrence of secondary cancer. The survival rate was calculated using the Kaplan-Meier method, and survival analysis was performed using the log-rank test. A difference was considered significant when the P value was less than 0.05 (*$P < 0.05$, **$P < 0.01$, and *** $P < 0.001$). All statistical analyses were performed using EZR (Saitama Medical Center, Jichi Medical University, Saitama, Japan), which is a graphical user interface for R (R Foundation for Statistical Computing, Vienna, Austria).

Results

Clinical implications of xCT and GPX4 expression in OSCC tissues before and after radiotherapy

We examined the expression levels of xCT and GPX4 in biopsy specimens obtained from 92 patients with OSCC by using immunohistochemical staining. Representative images of the expression patterns are shown in Fig. 1A. Classification into high or low expression was based on the semi-quantitative evaluation method described in the Materials and Methods section. The clinicopathological characteristics of the patients are presented in Supplementary Information Table S1. Of the 92 patients with OSCC, 34 (37.0%) and 35

(38.0%) showed high xCT and GPX4 expression levels, respectively. The relationships of the expression levels of xCT and GPX4 with OS and DFS were analyzed using the Kaplan-Meier method. High tumor expression levels of both xCT and GPX4 were significantly correlated with poor OS and DFS (Fig. 1B, C). Next, we immunohistochemically examined the expression levels of tumor xCT, GPX4, 4-HNE (lipid peroxidation marker), and Ki-67 (cellular proliferation marker) in surgical specimens containing surviving OSCC cells after 30 Gy of preoperative radiotherapy. Representative images illustrating their expression patterns are shown in Fig. 1D. The white dots are separate from the red and green dots, that is, the expression of 4-HNE was observed predominantly in xCT- and GPX4-negative tumor cells. These results suggest that upregulation of the molecules responsible for the ferroptosis defense system dampens the effects of radiotherapy.

Relationship of the expression levels of xCT and GPX4 with clinicopathological characteristics

There was a significant difference in the xCT expression status according to the primary site (Supplementary Information Table S1). There were no significant differences in the expression status of xCT or GPX4 by age, sex, pT category, pN category, clinical stage,

differentiation, mode of invasion, or pathological response to chemoradiotherapy (Supplementary Information Table S1). To explore the combination effects of xCT and GPX4 expression levels on the pathological response to chemoradiotherapy, we performed the same analysis using the combined variable, both xCT^{high} and $GPX4^{high}$ compared with either xCT^{low} or $GPX4^{low}$ (Supplementary Information Table S1). The variable xCT^{high} and $GPX4^{high}$ showed a significant correlation with poor pathological response to chemoradiotherapy.

Multivariate analysis of prognostic factors

Multivariate analysis using the Cox proportional hazards regression model revealed that pN category (hazard ratio, 3.803; $P < 0.01$), pathological response to chemoradiotherapy (hazard ratio, 0.195; $P < 0.001$), and GPX4 expression status (hazard ratio, 5.986; $P < 0.001$) were the significant prognostic factors for OS (Table 1). In addition, multivariate analysis for DFS demonstrated that the pN category (hazard ratio, 2.479; $P < 0.05$), mode of invasion (hazard ratio, 2.397; $P < 0.05$), pathological response to chemoradiotherapy (hazard ratio, 0.235; $P < 0.01$), and GPX4 expression status (hazard ratio, 4.818; $P < 0.001$) were the significant prognostic factors.

Radiation-induced cell death of OSCC cells is suppressed by ferrostatin-1 and potentiated by erastin and RSL3.

To confirm the involvement of ferroptosis in radiation-induced cell death in OSCC cells, we examined whether the ferroptosis inhibitor ferrostatin-1 and ferroptosis inducers erastin and RSL3 affected cell survival after a single 6 Gy dose of X-ray irradiation using a clonogenic assay. As shown in Figs. 2A and B, radiation caused a marked decrease in the surviving cells, and post-radiation survival was increased by ferrostatin-1 and decreased by erastin and RSL3 in the OSCC cell lines HSC-2 and HOC313. In addition, under the combined treatment of both a ferroptosis inducer and inhibitor, the cytocidal effect potentiated by radiation plus erastin or RSL3 was attenuated by ferrostatin-1 (Fig. 2A, B). These results indicate that ferroptosis is involved in radiation-induced cell death in OSCC cells.

Radiation-induced lipid peroxidation of OSCC cells is suppressed by ferrostatin-1 and deferoxamine, and potentiated by erastin and RSL3

Because ferroptosis is a form of cell death resulting from the accumulation of lipid peroxidation in cell membranes, we next evaluated lipid peroxidation after irradiation of OSCC cells using a detection probe for lipid peroxides. Twenty-four hours after

irradiation with 6 Gy, we observed significant radiation-induced lipid peroxidation compared to the control, which was enhanced by erastin and RSL3, and suppressed by ferrostatin-1 (Fig. 3A, B). In contrast, erastin and RSL3 caused a significant increase in lipid peroxidation without radiation, indicating that 2.5 μM erastin and 1 μM RSL3 used in our *in vitro* experiments functioned as ferroptosis inducers (Fig. 3C, D). Importantly, the iron chelator DFO suppressed radiation-, erastin-, and RSL3-induced lipid peroxidation (Fig. 3C, D), indicating that the suppression of lipid peroxidation by DFO was iron-dependent. Moreover, ferrostatin-1 suppressed erastin- and RSL3-induced lipid peroxidation in the absence of irradiation (Supplementary Information Fig. S1A, B), suggesting that the suppression of lipid peroxidation is associated with the inhibition of ferroptosis.

Radiation-induced ROS production by OSCC cells is potentiated by erastin and RSL3

Because ROS accumulation in cancer cells is closely related to ferroptosis, we examined intracellular ROS production levels in irradiated OSCC cells using the DCFH-DA reagent. Compared with the control, ROS levels were increased by radiation and further increased by radiation plus erastin or RSL3 (Fig. 4A, B). In addition, ROS levels induced by

radiation plus erastin or RSL3 were suppressed by ferrostatin-1 (Fig. 4A, B). In contrast, ROS production induced by radiation was not further suppressed by the addition of ferrostatin-1 (Fig. 4A, B), suggesting that ROS measurement using the DCFH-DA reagent detects ROS, but not lipid peroxidation, which is a characteristic of ferroptosis.

Erastin and RSL3 enhanced the effects of radiation on OSCC cells in a mouse xenograft model

We found that erastin and RSL3 increased the radiosensitivity of OSCC cells *in vitro*. Next, we examined the effect of radiation plus ferroptosis inducers on tumor growth of OSCC cells using a subcutaneous xenograft model. Because HOC313 cells lack the ability to engraft *in vivo*, we used HSC-2 cells in this experiment. The experimental protocol for evaluating antitumor effects *in vivo* is shown in Fig. 5A. As shown in Fig. 5B, radiation alone significantly suppressed tumor growth compared with the control; erastin alone exhibited a weak but significant suppressive effect at this dosage level. In addition, we confirmed that radiation plus erastin significantly suppressed the tumor volume compared to radiation alone (Fig. 5B). In contrast, as shown in Fig. 5C, radiation alone significantly suppressed tumor growth compared to the control; RSL3 alone did not exhibit a significant suppressive effect at this dose. Moreover, we confirmed that radiation

plus RSL3 significantly suppressed the tumor volume compared to radiation alone (Fig. 5C). Despite the potent anticancer effects, there was a minimal difference in the weight between mice in the treated and untreated groups (Supplementary Information Fig. S2A, B). After the mice were sacrificed on day 29, we observed the tumor characteristics by immunohistochemical analyses of the proliferation marker Ki-67 and lipid peroxidation marker 4-HNE (Fig. 5D). Histopathological analysis revealed that the tumor cells and tissue structures were damaged by radiation, and the irreversible or lethal effects were potentiated by erastin and RSL3, despite the low efficacy of a single administration. On immunohistochemical analyses, the percentage of Ki-67-positive cells was markedly decreased in the group treated with radiation combined with erastin or RSL3 (Fig. 5D); in contrast, the percentage of 4-HNE-positive cells increased considerably in the groups treated with radiation combined with erastin or RSL3 (Fig. 5D).

Discussion

In this study, high immunohistochemical expression of xCT and GPX4 in OSCC tissues was significantly correlated with a shorter OS and DFS (Fig. 1B, C). Multivariate analysis revealed that high GPX4 expression was an independent predictor of poor prognosis (Table 1). To the best of our knowledge, this is the first report of an association between

tumor GPX4 expression and poor prognosis in patients with HNSCC. In concordance with our results, tumor GPX4 overexpression has been reported to be an independent poor prognostic predictor in lung adenocarcinoma[26] and diffuse large B-cell lymphoma.[27] Furthermore, *GPX4* has been shown to act as an oncogene and is negatively associated with the prognosis in many cancers.[28] With regard to xCT, consistent with the result of our univariate analysis, it has been reported that xCT expression is associated with a more unfavorable prognosis in many cancers, including OSCC.[29, 30] Our multivariate analysis may have failed to reveal a significant association between xCT expression and unfavorable prognosis owing to the differences in sample size, epitope retrieval method, and evaluation criteria. However, a central regulator GPX4 in ferroptosis-defensive xCT/GPX4 axis significantly influences the clinical outcomes of patients with OSCC.

Although radiation-induced cell death involves various forms of cell death, including apoptosis, necroptosis, and mitotic catastrophes,[31, 32] the importance of ferroptosis in cancer radiotherapy remains unclear. However, as shown in Fig. 2, treatment with the ferroptosis inhibitor ferrostatin-1 partially increased survival, which was reduced by radiation. In addition, the apoptosis inhibitor Z-VAD and necroptosis inhibitor necrostatin-1s restored survival after radiation to the same extent (data not shown). These results indicate that ferroptosis, apoptosis, and necroptosis are all forms of

radiation-induced cell death in OSCC cells. This suggests that radiotherapy combined with ferroptosis inducers may be able to enhance the efficacy of radiotherapy.

We demonstrated that erastin and RSL3 potentiated the antitumor effects of irradiation in OSCC cells *in vitro* and *in vivo* (Fig. 2 and 5). We also confirmed that reduced clonogenic survival due to radiation was followed by increased lipid peroxidation (Fig. 3A, B), and ferroptotic lipid peroxidation was suppressed by DFO (Fig. 3C, D). Furthermore, suppressed tumor growth *in vivo* was followed by decreased Ki-67 expression and increased 4-HNE expression (Fig. 5D). Collectively, our data indicate that the abrogation of the xCT/GPX4 axis using ferroptosis inhibitors potentiates the effects of radiotherapy. With regard to the involvement of ferroptosis in the effect of radiation, our results are in agreement with those of previous reports.[5-7] It has been revealed that immunotherapy-activated $CD8^+$ T cells can enhance tumor lipid peroxidation and ferroptosis.[5, 33] The effect is mechanistic because interferon gamma released from $CD8^+$ T cells downregulates the expression of xCT, resulting in reduced cystine uptake.[5, 33] As mentioned above, ferroptosis is known to affect the outcomes of not only radiotherapy, but also immunotherapy, and the xCT/GPX4 axis plays an important role in it. Taken together, ferroptosis induction by targeting the xCT/GPX4 axis is a promising and novel strategy for cancer therapy.

With respect to safety evaluation of ferroptosis inducers, erastin and RSL3, no significant body weight reduction and observable signs of toxicity were observed in our xenograft model, consistent with previous reports.[18, 34, 35] Reportedly, no in vivo toxicity was confirmed in intraperitoneal injection of RSL-3 up to 400 mg/kg dose, suggesting that these doses of RSL-3 were well tolerated.[18] Conversely, erastin-induced ferroptisis was reported to cause physiological and pathological changes in healthy tissues of mice, suggesting that erastin was somewhat toxic to healthy tissues.[36] In the study, mice were intraperitoneally injected a 25 mg/kg dose of erastin at 12-h intervals for 2 days. In our study, however, mice were intraperitoneally injected with a 15 mg/kg dose of erastin at 24-h intervals for 10 days. Therefore, the potential adverse effects associated with erastin administration appeared to be attributable to the dosing regimen.

Although GPX4 is capable of converting PL hydroperoxides to PL alcohols,[37] and is regarded as a pivotal suppressor of ferroptosis,[14, 38] some cancer cells that express low levels of GPX4 remain resistant to ferroptosis,[39] suggesting the presence of another ferroptosis defense system. Ferroptosis suppressor protein 1 (FSP1; also known as AIFM2) operates in parallel with GPX4 to defend against ferroptosis.[40, 41] FSP functions as an NAD(P)H-dependent oxidoreductase capable of reducing CoQ (also known as coenzyme Q or ubiquinone) to $CoQH_2$ (ubiquinol).[40, 41] $CoQH_2$ can trap lipid peroxyl

radicals, thereby suppressing lipid peroxidation and ferroptosis.[38] Thus, the FSP/$CoQH_2$ axis is a recently established alternative ferroptosis defense system. One major limitation of our study is that the involvement of the FSP/$CoQH_2$ axis was not considered. Importantly, the FSP/$CoQH_2$ axis acts independently in concert with the xCT/GPX4 axis.[14] Therefore, further analyses are required to uncover the involvement of the FSP/$CoQH_2$ axis in the antitumor effects of radiation in OSCC.

Conclusions

In conclusion, we demonstrated for the first time that tumor GPX4 expression is an independent predictor of poor prognosis in patients with OSCC. Our data indicate that the xCT/GPX4 axis is involved in radiation-mediated antitumor effects in OSCC and that radiotherapy combined with ferroptosis induction by targeting the xCT/GPX4 axis may improve the prognosis of patients with advanced HNSCC, including OSCC.

References

1. Caudell JJ, Torres-Roca JF, Gillies RJ, Enderling H, Kim S, Rishi A, et al. The future of personalised radiotherapy for head and neck cancer. Lancet Oncol 2017; 18(5):e266-e73.

2. Cabrera-Licona A, Pérez-Añorve IX, Flores-Fortis M, Moral-Hernández OD, González-de la Rosa CH, Suárez-Sánchez R, et al. Deciphering the epigenetic network in cancer radioresistance. Radiother Oncol 2021; 159:48-59.

3. Larionova I, Rakina M, Ivanyuk E, Trushchuk Y, Chernyshova A, Denisov E. Radiotherapy resistance: identifying universal biomarkers for various human cancers. J Cancer Res Clin Oncol 2022; 148(5):1015-31.
4. Kuwahara Y, Tomita K, Urushihara Y, Sato T, Kurimasa A, Fukumoto M. Association between radiation-induced cell death and clinically relevant radioresistance. Histochem Cell Biol 2018; 150(6):649-59.
5. Lang X, Green MD, Wang W, Yu J, Choi JE, Jiang L, et al. Radiotherapy and Immunotherapy Promote Tumoral Lipid Oxidation and Ferroptosis via Synergistic Repression of SLC7A11. Cancer Discov 2019; 9(12):1673-85.
6. Lei G, Zhang Y, Koppula P, Liu X, Zhang J, Lin SH, et al. The role of ferroptosis in ionizing radiation-induced cell death and tumor suppression. Cell Res 2020; 30(2):146-62.
7. Ye LF, Chaudhary KR, Zandkarimi F, Harken AD, Kinslow CJ, Upadhyayula PS, et al. Radiation-induced lipid peroxidation triggers ferroptosis and synergizes with ferroptosis inducers. ACS Chem Biol 2020; 15(2):469-84.
8. Azzam EI, Jay-Gerin JP, Pain D. Ionizing radiation-induced metabolic oxidative stress and prolonged cell injury. Cancer Lett 2012; 327(1-2):48-60.
9. Shadyro OI, Yurkova IL, Kisel MA. Radiation-induced peroxidation and fragmentation of lipids in a model membrane. Int J Radiat Biol 2002; 78(3):211-7.
10. Doll S, Proneth B, Tyurina YY, Panzilius E, Kobayashi S, Ingold I, et al. ACSL4 dictates ferroptosis sensitivity by shaping cellular lipid composition. Nat Chem Biol 2017; 13(1):91-8.
11. Kagan VE, Mao G, Qu F, Angeli JP, Doll S, Croix CS, et al. Oxidized arachidonic and adrenic PEs navigate cells to ferroptosis. Nat Chem Biol 2017; 13(1):81-90.
12. Yang WS, Kim KJ, Gaschler MM, Patel M, Shchepinov MS, Stockwell BR. Peroxidation of polyunsaturated fatty acids by lipoxygenases drives ferroptosis. Proc Natl Acad Sci U S A 2016; 113(34):E4966-75.
13. Dixon SJ, Lemberg KM, Lamprecht MR, Skouta R, Zaitsev EM, Gleason CE, et al. Ferroptosis: an iron-dependent form of nonapoptotic cell death. Cell 2012; 149(5):1060-72.
14. Lei G, Mao C, Yan Y, Zhuang L, Gan B. Ferroptosis, radiotherapy, and combination therapeutic strategies. Protein Cell 2021; 12(11):836-57.
15. Koppula P, Zhuang L, Gan B. Cystine transporter SLC7A11/xCT in cancer: ferroptosis, nutrient dependency, and cancer therapy. Protein Cell 2021; 12(8):599-620.
16. Stockwell BR. Ferroptosis turns 10: Emerging mechanisms, physiological functions, and therapeutic applications. Cell 2022; 185(14):2401-21.

17. Stockwell BR, Friedmann Angeli JP, Bayir H, Bush AI, Conrad M, Dixon SJ, et al. Ferroptosis: A regulated cell death nexus linking metabolism, redox biology, and disease. Cell 2017; 171(2):273-85.
18. Yang WS, SriRamaratnam R, Welsch ME, Shimada K, Skouta R, Viswanathan VS, et al. Regulation of ferroptotic cancer cell death by GPX4. Cell 2014; 156(1-2):317-31.
19. Skouta R, Dixon SJ, Wang J, Dunn DE, Orman M, Shimada K, et al. Ferrostatins inhibit oxidative lipid damage and cell death in diverse disease models. J Am Chem Soc 2014; 136(12):4551-6.
20. Shibata Y, Yasui H, Higashikawa K, Miyamoto N, Kuge Y. Erastin, a ferroptosis-inducing agent, sensitized cancer cells to X-ray irradiation via glutathione starvation in vitro and in vivo. PloS one 2019; 14(12):e0225931.
21. Cui Y, Zhang Z, Zhou X, Zhao Z, Zhao R, Xu X, et al. Microglia and macrophage exhibit attenuated inflammatory response and ferroptosis resistance after RSL3 stimulation via increasing Nrf2 expression. Journal of neuroinflammation 2021; 18(1):249.
22. Nagata M, Nakayama H, Tanaka T, Yoshida R, Yoshitake Y, Fukuma D, et al. Overexpression of cIAP2 contributes to 5-FU resistance and a poor prognosis in oral squamous cell carcinoma. British journal of cancer 2011; 105(9):1322-30.
23. Yoshida R, Nakayama H, Nagata M, Hirosue A, Tanaka T, Kawahara K, et al. Overexpression of nucleostemin contributes to an advanced malignant phenotype and a poor prognosis in oral squamous cell carcinoma. Br J Cancer 2014; 111(12):2308-15.
24. Matsuoka Y, Yoshida R, Kawahara K, Sakata J, Arita H, Nakashima H, et al. The antioxidative stress regulator Nrf2 potentiates radioresistance of oral squamous cell carcinoma accompanied with metabolic modulation. Lab Invest 2022; 102(8):896-907.
25. Shimosato YO, S.; Baba, K. Histological evaluation of effects of radiotherapy and chemotherapy for carcinomas. Jap J Clin Oncol 1971; 1(1):19-35.
26. Liu CY, Liu CC, Li AF, Hsu TW, Lin JH, Hung SC, et al. Glutathione peroxidase 4 expression predicts poor overall survival in patients with resected lung adenocarcinoma. Sci Rep 2022; 12(1):20462.
27. Kinowaki Y, Kurata M, Ishibashi S, Ikeda M, Tatsuzawa A, Yamamoto M, et al. Glutathione peroxidase 4 overexpression inhibits ROS-induced cell death in diffuse large B-cell lymphoma. Lab Invest 2018; 98(5):609-19.
28. Zhang X, Sui S, Wang L, Li H, Zhang L, Xu S, et al. Inhibition of tumor propellant glutathione peroxidase 4 induces ferroptosis in cancer cells and enhances anticancer effect of cisplatin. J Cell Physiol 2020; 235(4):3425-37.
29. Wang J, Hao S, Song G, Wang Y, Hao Q. The prognostic and clinicopathological

significance of SLC7A11 in human cancers: a systematic review and meta-analysis. PeerJ 2023; 11:e14931.
30. Lee JR, Roh JL, Lee SM, Park Y, Cho KJ, Choi SH, et al. Overexpression of cysteine-glutamate transporter and CD44 for prediction of recurrence and survival in patients with oral cavity squamous cell carcinoma. Head Neck 2018; 40(11):2340-6.
31. Jiao Y, Cao F, Liu H. Radiation-induced cell death and its mechanisms. Health Phys 2022; 123(5):376-86.
32. Galluzzi L, Vitale I, Aaronson SA, Abrams JM, Adam D, Agostinis P, et al. Molecular mechanisms of cell death: recommendations of the Nomenclature Committee on Cell Death 2018. Cell Death Differ 2018; 25(3):486-541.
33. Wang W, Green M, Choi JE, Gijon M, Kennedy PD, Johnson JK, et al. $CD8^+$ T cells regulate tumour ferroptosis during cancer immunotherapy. Nature 2019; 569(7755):270-4.
34. Ghoochani A, Hsu EC, Aslan M, Rice MA, Nguyen HM, Brooks JD, et al. Ferroptosis Inducers Are a Novel Therapeutic Approach for Advanced Prostate Cancer. Cancer Res 2021; 81(6):1583-94.
35. Huo H, Zhou Z, Qin J, Liu W, Wang B, Gu Y. Erastin Disrupts Mitochondrial Permeability Transition Pore (mPTP) and Induces Apoptotic Death of Colorectal Cancer Cells. PLoS One 2016; 11(5):e0154605.
36. Zhao J, Xu B, Xiong Q, Feng Y, Du H. Erastin-induced ferroptosis causes physiological and pathological changes in healthy tissues of mice. Mol Med Rep 2021; 24(4).
37. Seibt TM, Proneth B, Conrad M. Role of GPX4 in ferroptosis and its pharmacological implication. Free Radic Biol Med 2019; 133:144-52.
38. Lei G, Zhuang L, Gan B. Targeting ferroptosis as a vulnerability in cancer. Nat Rev Cancer 2022; 22(7):381-96.
39. Viswanathan VS, Ryan MJ, Dhruv HD, Gill S, Eichhoff OM, Seashore-Ludlow B, et al. Dependency of a therapy-resistant state of cancer cells on a lipid peroxidase pathway. Nature 2017; 547(7664):453-7.
40. Bersuker K, Hendricks JM, Li Z, Magtanong L, Ford B, Tang PH, et al. The CoQ oxidoreductase FSP1 acts parallel to GPX4 to inhibit ferroptosis. Nature 2019; 575(7784):688-92.
41. Doll S, Freitas FP, Shah R, Aldrovandi M, da Silva MC, Ingold I, et al. FSP1 is a glutathione-independent ferroptosis suppressor. Nature 2019; 575(7784):693-8.

Figure legends

Figure 1

High tumor expression levels of xCT and GPX4 are associated with unfavorable outcomes in patients with advanced oral squamous cell carcinoma (OSCC).

The expression of xCT and GPX4 by immunohistochemical staining of tumor biopsy specimens obtained from 92 patients with advanced OSCC was quantified by the staining intensity and positivity rate, and classified into two groups: high expression and low expression groups. (A) Representative images showing high and low expression patterns of xCT and GPX4. Scale bar, 50 μm. Overall survival (OS) and disease-free survival (DFS) of 92 patients with OSCC based on the expression levels of xCT (B) and GPX4 (C) were calculated using the Kaplan-Meier method, and the statistical differences in survival among subgroups of patients were compared using the log-rank test. $*P < 0.05$, $**P < 0.01$, $***P < 0.001$. (D) Representative images of the simultaneous detection of xCT (red), GPX4 (green), 4-HNE (white), and DAPI (blue) in irradiated OSCC tissues using multiplex fluorescent immunohistochemistry. “Merge” represents the overlay image of xCT, GPX4, and 4-HNE. Black scale bar, 50 μm. Yellow scale bar, 50 μm.

Figure 2

Radiation-induced death of oral squamous cell carcinoma (OSCC) cells is suppressed by ferrostatin-1 and potentiated by erastin and RSL3.

Cell survival was evaluated using the clonogenic assay. HSC-2 (A) and HOC313 (B) cells were pretreated with 5 μM ferrostatin-1, 2.5 μM erastin, 2.5 μM erastin plus 5 μM ferrostatin-1, 1 μM RSL3, or 1 μM RSL3 plus 5 μM ferrostatin-1 for 24 h followed by a single 6 Gy dose of X-ray irradiation. After irradiation, the cells were transferred to gelatin-coated 60 mm culture dishes and incubated. After 10 days, the cells were fixed and visualized. Representative images of each group and the corresponding bar graphs are shown. The results are shown as the means ± SE of three independent experiments. *P* values were calculated using two-tailed unpaired Student's *t*-test. $*P < 0.05$.

Figure 3

Radiation-induced lipid peroxidation of oral squamous cell carcinoma (OSCC) cells is suppressed by ferrostatin-1 and deferoxamine, and potentiated by erastin and RSL3.

Lipid peroxidation was evaluated using Liperflo reagent. After a single 6 or 0 Gy dose of X-ray irradiation, HSC-2 (A, C) and HOC313 (B, D) cells were treated with 5 μM ferrostatin-1, 2.5 μM erastin, 2.5 μM erastin plus 5 μM ferrostatin-1, 1 μM RSL3, 1 μM

RSL3 plus 5 μM ferrostatin-1, or 30 μM deferoxamine (DFO). After 24 h, the cells were exposed to Liperfluo for lipid peroxide detection and observed under a fluorescence microscope. Representative fluorescence images of each group and the corresponding bar graphs are shown. Liperfluo fluorescence intensity was analyzed by measuring at least 200 cells using ImageJ software. The results are shown as the means ± SE of three independent experiments. *P* values were calculated using two-tailed unpaired Student's *t*-test. ***$P < 0.001$.

Figure 4

Radiation-induced reactive oxygen species (ROS) production in oral squamous cell carcinoma (OSCC) cells is potentiated by erastin and RSL3.

Intracellular ROS levels were evaluated using highly sensitive DCFH-DA. After a single 6 Gy dose of X-ray irradiation, HSC-2 (A) and HOC313 (B) cells were treated with 5 μM ferrostatin-1, 2.5 μM erastin, 2.5 μM erastin plus 5 μM ferrostatin-1, 1 μM RSL3, or 1 μM RSL3 plus 5 μM ferrostatin-1. After 24 h, the cells were exposed to DCFH-DA solution, and the fluorescence intensity due to ROS was measured using a microplate reader and visualized using a microscope. Representative fluorescence images of each group and the corresponding bar graphs are shown. The results are shown as the

means ± SE of three independent experiments. *P* values were calculated using two-tailed unpaired Student's *t*-test. ***$P < 0.001$.

Figure 5

Erastin and RSL3 enhanced the effects of radiation on oral squamous cell carcinoma (OSCC) cells in a mouse xenograft model.

(A) The experimental protocol for evaluating anti-tumor effects of erastin and RSL3 using a xenograft model. Nude mice were implanted with subcutaneous HSC-2 cells to form xenograft tumors. The experiment was initiated when the tumor size reached approximately 100 mm^3. Erastin or RSL3 were intraperitoneally injected at a dose of 15 or 5 mg/kg/day, respectively, for 10 days at 24-hour intervals. For radiotherapy, anesthetized mice were locally irradiated with a single 3 Gy dose of X-ray/day for 10 days. (B) Images of the mice after treatment with control, erastin alone, irradiation (IR) alone (30 Gy), and combination of IR (30 Gy) plus erastin, and the corresponding line graph of the tumor volume are shown. (C) Images of the mice after treatment with control, RSL3 alone, IR alone (30 Gy), and combination of IR (30 Gy) plus RSL3, and the corresponding line graph of the tumor volume are shown. Tumor size in each group was measured every other day using a caliper. Tumor volume was calculated as V (mm^3) = (L

$\times W^2)/2$. The results are shown as the means ± SE of three independent experiments. *P* values were calculated using two-tailed unpaired Student's *t*-test. **P* < 0.05, ***P* < 0.01, ****P* < 0.001. (D) Representative microscopic images of hematoxylin eosin (HE) and immunohistochemical staining for the proliferation marker Ki-67 and lipid peroxidation marker 4-HNE in the tumor specimens. Bar, 50 μm. The percentages of Ki-67 and 4HNE positive cells counted in 5 randomized fields in specimens from each group are shown. The results are presented as the means ± SE of three independent experiments. **P* < 0.05, ***P* < 0.01.

Table 1

Multivariate regression analysis of overall survival (OS) and disease-free survival (DFS) in patients (n=92) with oral squamous cell carcinoma (OSCC)

Supplementary Information

Supplementary Information Figure S1

Ferrostatin-1 suppresses erastin- and RSL3-induced lipid peroxidation without radiation.

Lipid peroxidation was evaluated using Liperflo reagent. HSC-2 (A) and HOC313 (B)

cells were treated with 5 μM ferrostatin-1, 2.5 μM erastin, 2.5 μM erastin plus 5 μM ferrostatin-1, 1 μM RSL3, and 1 μM RSL3 plus 5 μM ferrostatin-1. After 24 h, the cells were exposed to Liperfluo and observed under a fluorescence microscope. Representative fluorescence images of each group and the corresponding bar graphs are shown. Liperfluo fluorescence intensity was analyzed by measuring at least 200 cells using ImageJ software. The results are shown as the means ± SE of three independent experiments. *P* values were calculated using two-tailed unpaired Student's *t*-test. ***$P < 0.001$.

Supplementary Information Figure S2

Body weight measurement of tumor-implanted mice during the *in vivo* experiment.

(A, B) The weights of the mice were measured every other day for 25 days. The results are shown as the means ± SE of three independent experiments.

Supplementary Information Table S1

Distribution of xCT and GPX4 expression levels in patients (n=92) with oral squamous cell carcinoma (OSCC) according to the clinicopathological characteristics.

Figure 1

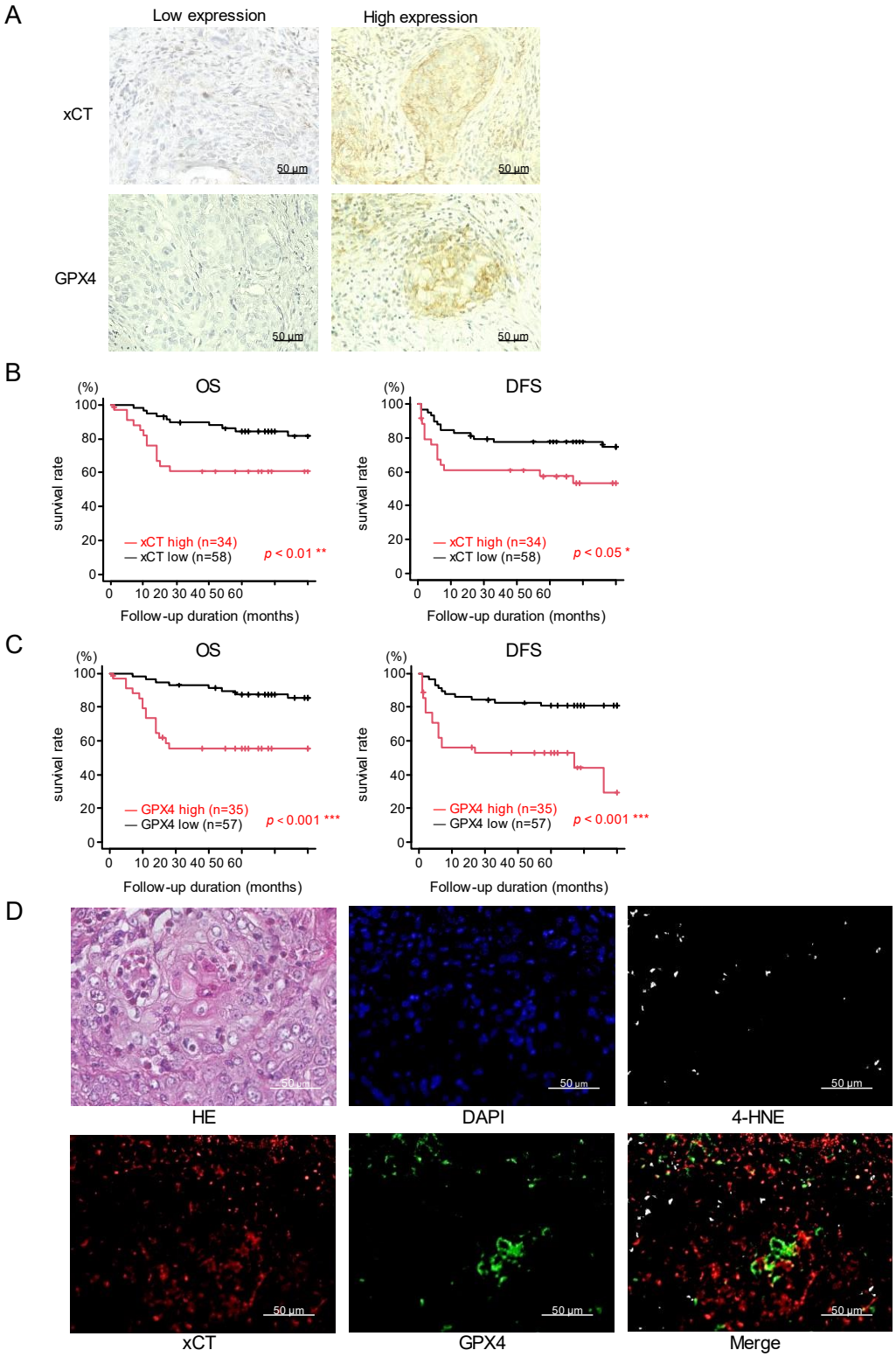
A
Low expression
High expression
xCT
GPX4
50 μm
B
OS
DFS
(%)
survival rate
— xCT high (n=34)
— xCT low (n=58)
p < 0.01 **
p < 0.05 *
Follow-up duration (months)
C
— GPX4 high (n=35)
— GPX4 low (n=57)
p < 0.001 ***
D
HE
DAPI
4-HNE
xCT
GPX4
Merge

Figure 2

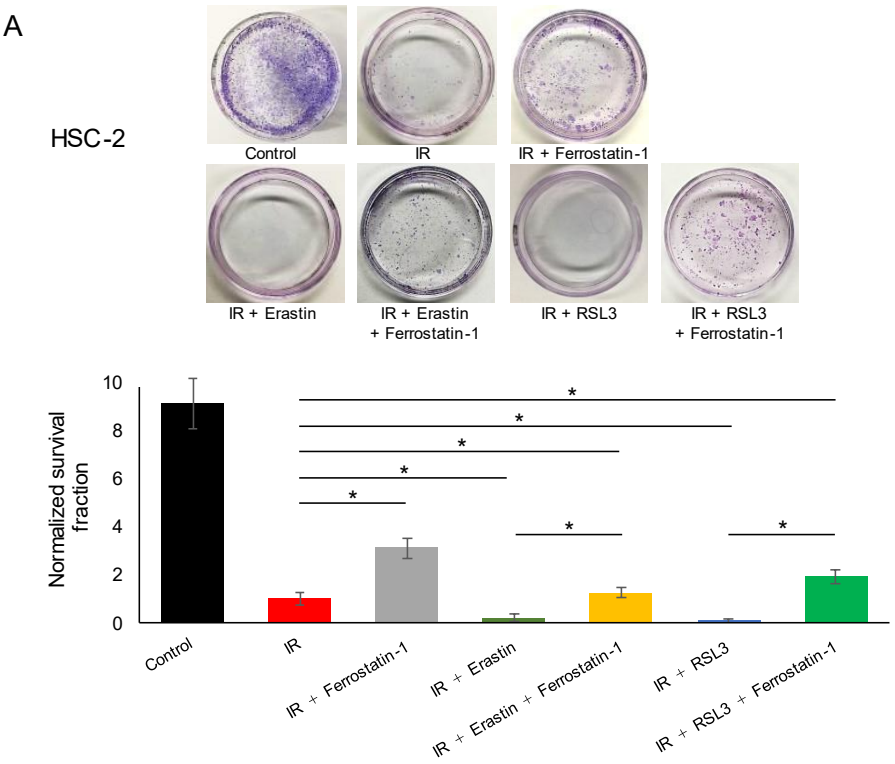
A
HSC-2
Control
IR
IR + Ferrostatin-1
IR + Erastin
IR + Erastin + Ferrostatin-1
IR + RSL3
IR + RSL3 + Ferrostatin-1
Normalized survival fraction
0
2
4
6
8
10
*
Control
IR
IR + Ferrostatin-1
IR + Erastin
IR + Erastin + Ferrostatin-1
IR + RSL3
IR + RSL3 + Ferrostatin-1

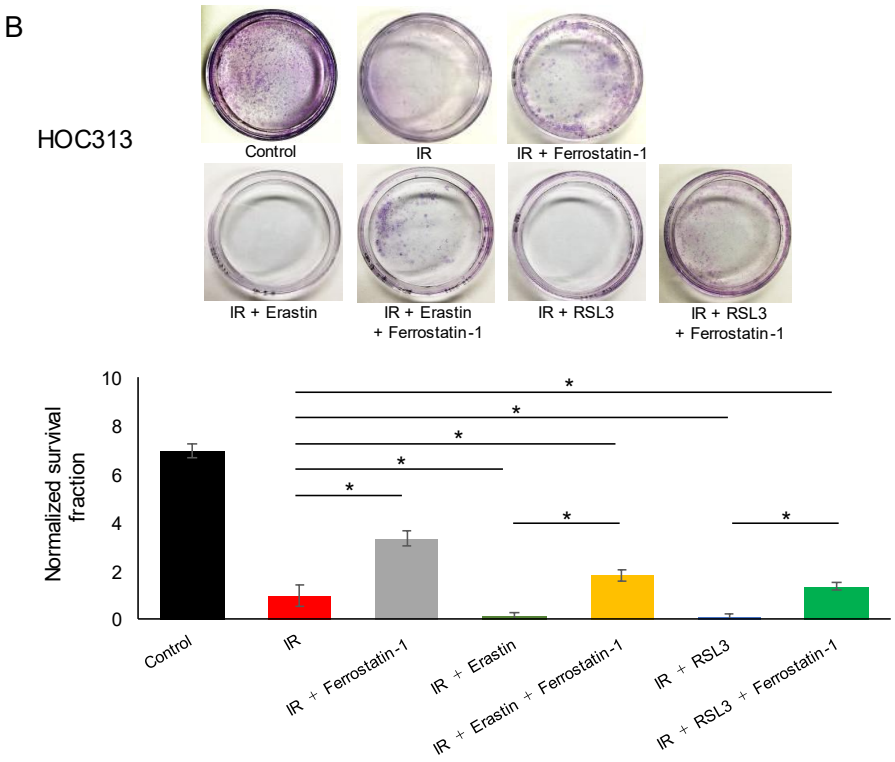
B
HOC313
Control
IR
IR + Ferrostatin-1
IR + Erastin
IR + Erastin + Ferrostatin-1
IR + RSL3
IR + RSL3 + Ferrostatin-1
Normalized survival fraction
0
2
4
6
8
10
*
Control
IR
IR + Ferrostatin-1
IR + Erastin
IR + Erastin + Ferrostatin-1
IR + RSL3
IR + RSL3 + Ferrostatin-1

Figure 3

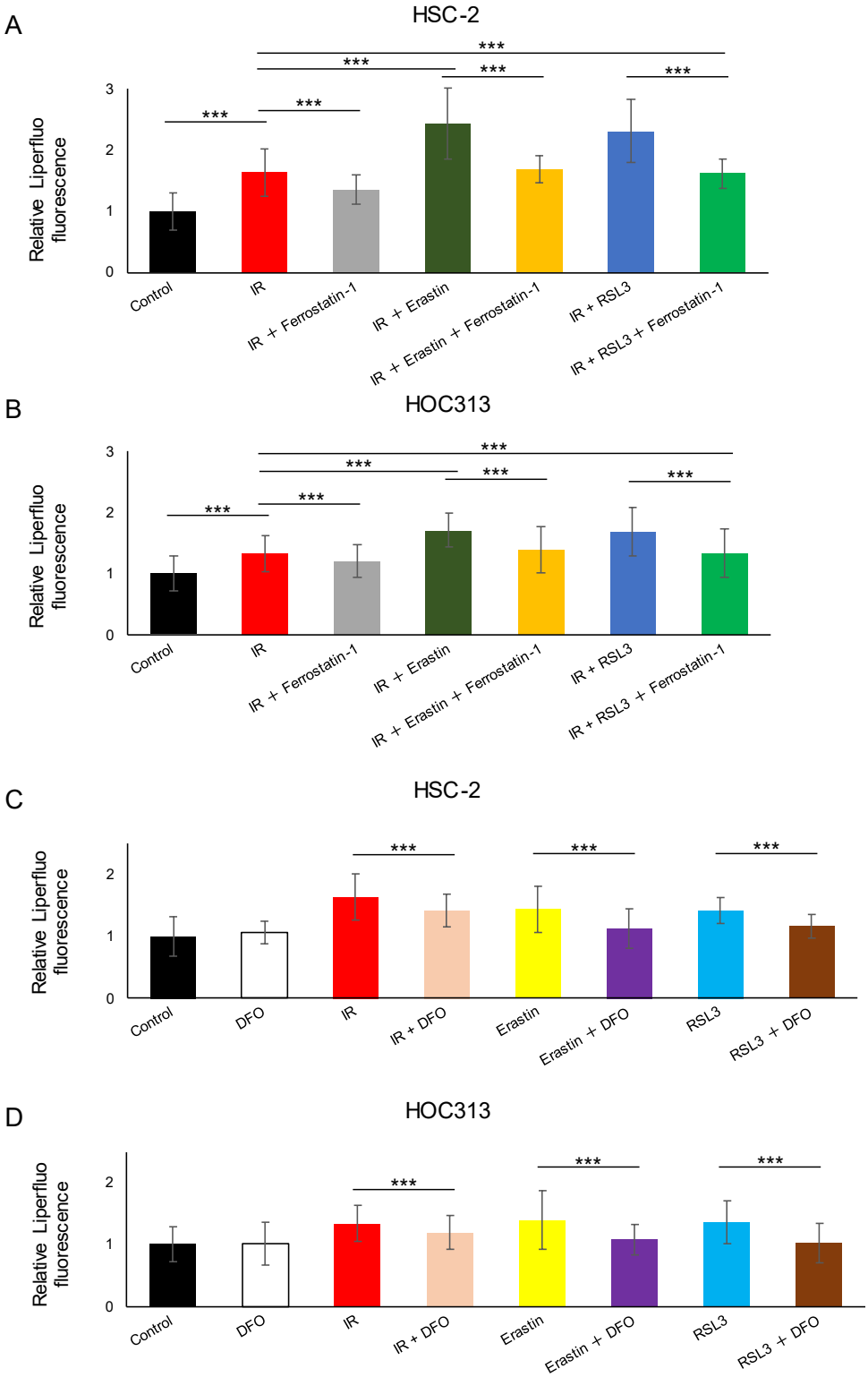
A
HSC-2
Relative Liperfluo fluorescence
0
1
2
3
***
Control
IR
IR + Ferrostatin-1
IR + Erastin
IR + Erastin + Ferrostatin-1
IR + RSL3
IR + RSL3 + Ferrostatin-1
B
HOC313
C
HSC-2
DFO
IR + DFO
Erastin
Erastin + DFO
RSL3
RSL3 + DFO
D
HOC313

Figure 4

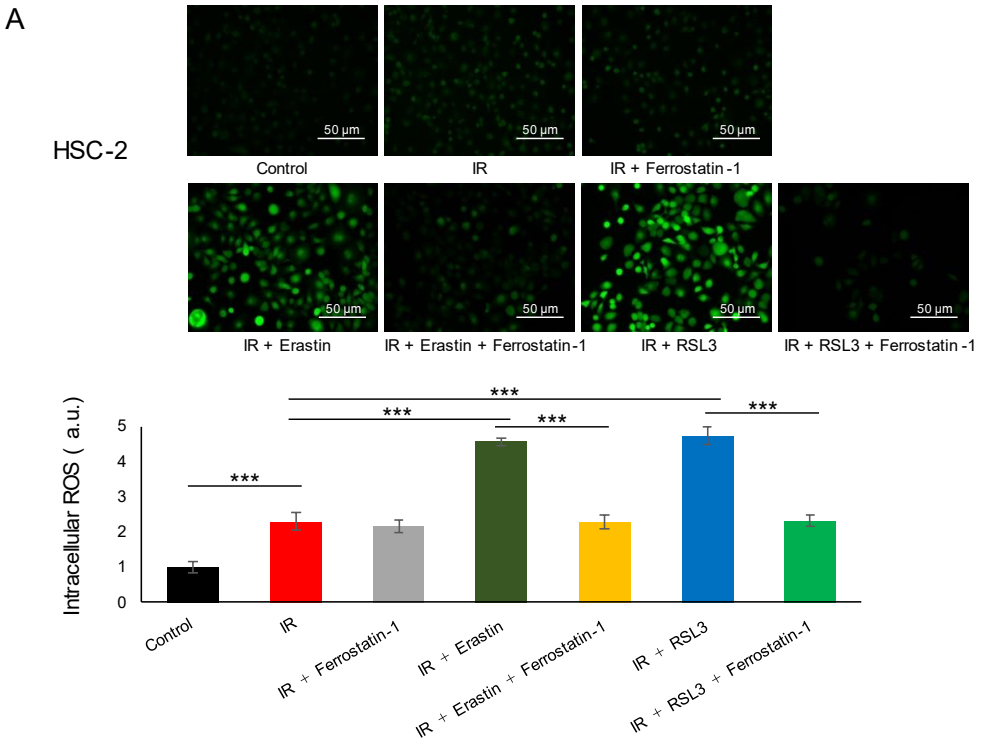
A
HSC-2
50 μm
Control
IR
IR + Ferrostatin-1
IR + Erastin
IR + Erastin + Ferrostatin-1
IR + RSL3
IR + RSL3 + Ferrostatin-1
Intracellular ROS (a.u.)
0
1
2
3
4
5
***
Control
IR
IR + Ferrostatin-1
IR + Erastin
IR + Erastin + Ferrostatin-1
IR + RSL3
IR + RSL3 + Ferrostatin-1

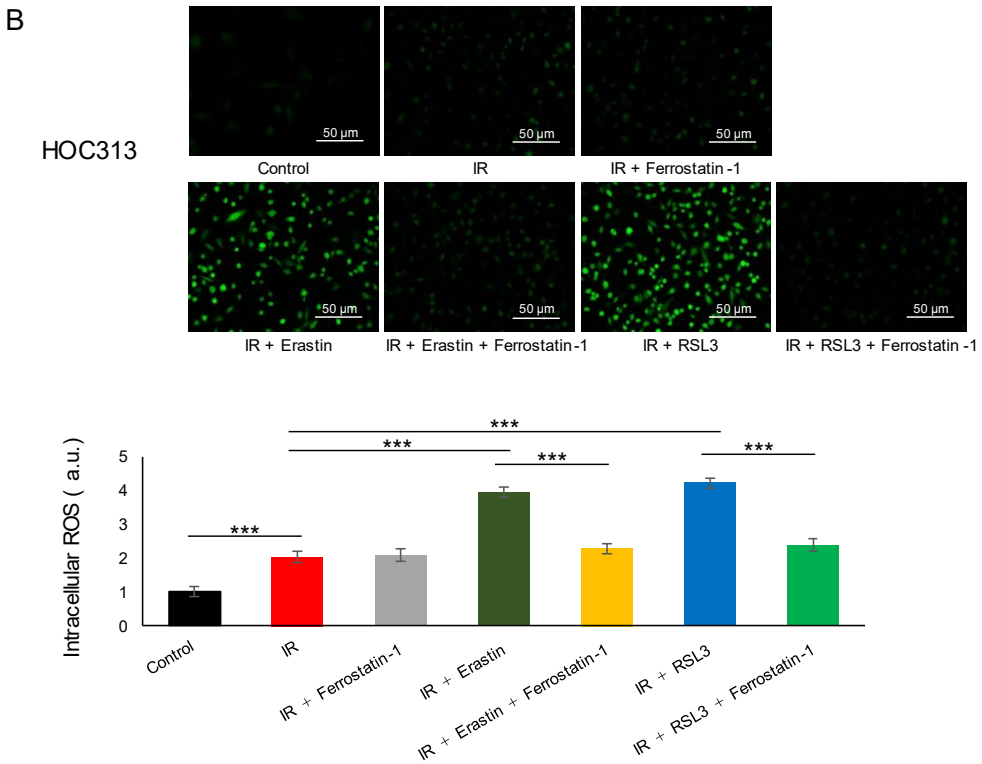
B
HOC313
50 μm
Control
IR
IR + Ferrostatin-1
IR + Erastin
IR + Erastin + Ferrostatin-1
IR + RSL3
IR + RSL3 + Ferrostatin-1
Intracellular ROS (a.u.)
0
1
2
3
4
5
***
Control
IR
IR + Ferrostatin-1
IR + Erastin
IR + Erastin + Ferrostatin-1
IR + RSL3
IR + RSL3 + Ferrostatin-1

Figure 5

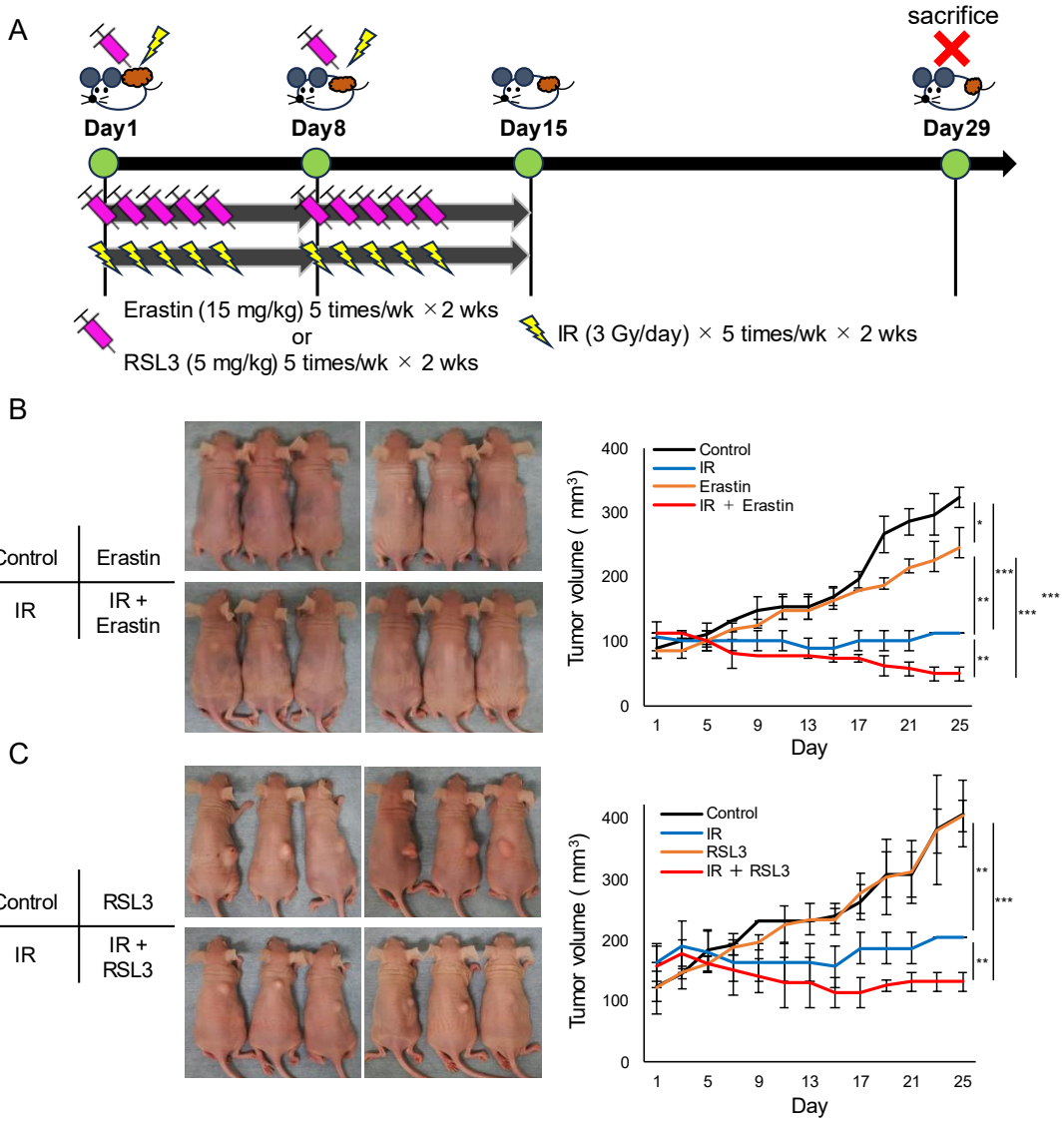
A
sacrifice
Day1
Day8
Day15
Day29
Erastin (15 mg/kg) 5 times/wk ×2 wks
or
RSL3 (5 mg/kg) 5 times/wk × 2 wks
IR (3 Gy/day) × 5 times/wk × 2 wks
B
Control
Erastin
IR
IR + Erastin
Control
IR
Erastin
IR + Erastin
Tumor volume (mm3)
Day
C
Control
RSL3
IR
IR + RSL3
Control
IR
RSL3
IR + RSL3
Tumor volume (mm3)
Day

Figure 5

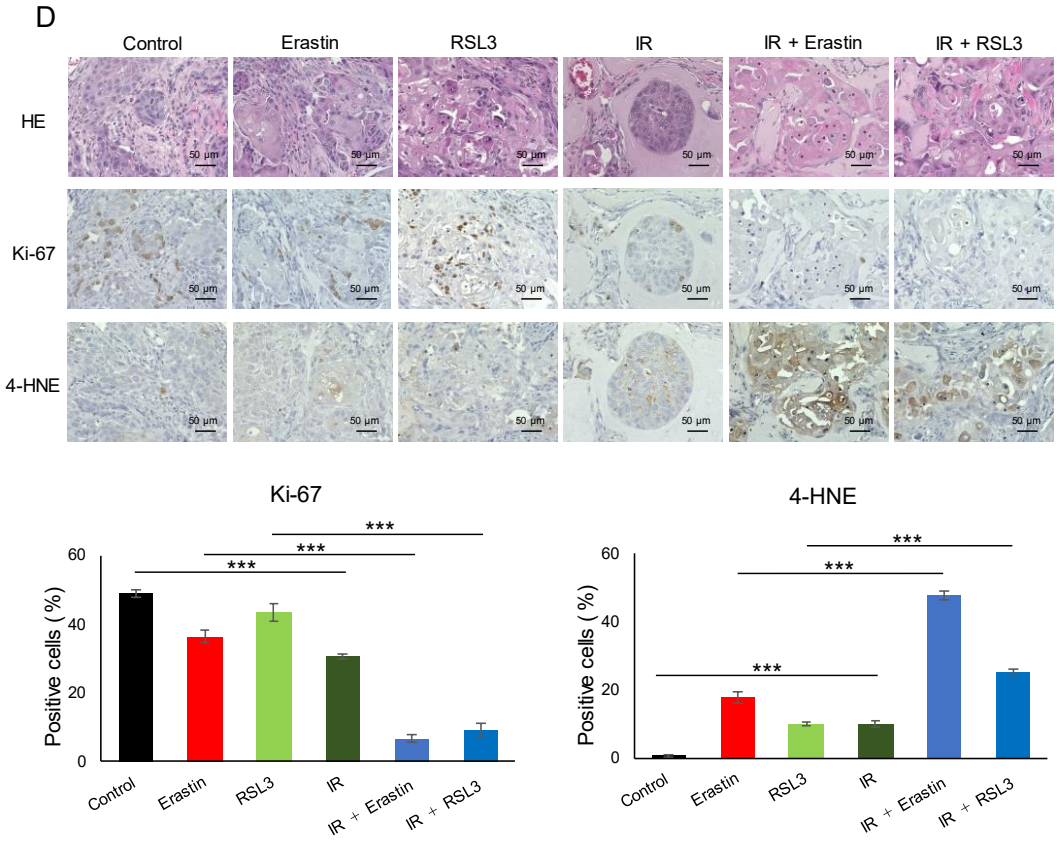
D
Control
Erastin
RSL3
IR
IR + Erastin
IR + RSL3
HE
Ki-67
4-HNE
50 μm
Ki-67
Positive cells (%)
60
40
20
0
***
***
***
Control
Erastin
RSL3
IR
IR + Erastin
IR + RSL3
4-HNE
Positive cells (%)
60
40
20
0
***
***
***
Control
Erastin
RSL3
IR
IR + Erastin
IR + RSL3

Table 1

Variables	Assigned score	OS		DFS	
		Hazard ratio (95% CI)	*P*-value	Hazard ratio (95% CI)	*P*-value
pN category					
N0	0	7.273 (2.512-21.060)	< 0.001***	4.310 (1.836 -10.120)	< 0.010**
N1, N2	1				
Mode of invasion					
Grade I, II, III	0	1.821 (0.675 -4.227)	0.189	2.695 (1.187-6.121)	< 0.050*
Grade IV	1				
Pathological response					
Grade 0, I, IIa, IIb	0	0.110 (0.037- 0.324)	< 0.001***	0.120 (0.047-0.308)	< 0.001***
Grade III, IV	1				
xCT status					
Low	0	1.025 (0.349-3.011)	0.963	0.677 (0.264-1.737)	0.418
High	1				
GPX4 status					
Low	0	6.972 (2.210-21.990)	< 0.001***	5.514 (2.124-14.320)	< 0.001***
High	1				

Supplementary Information Figure S1

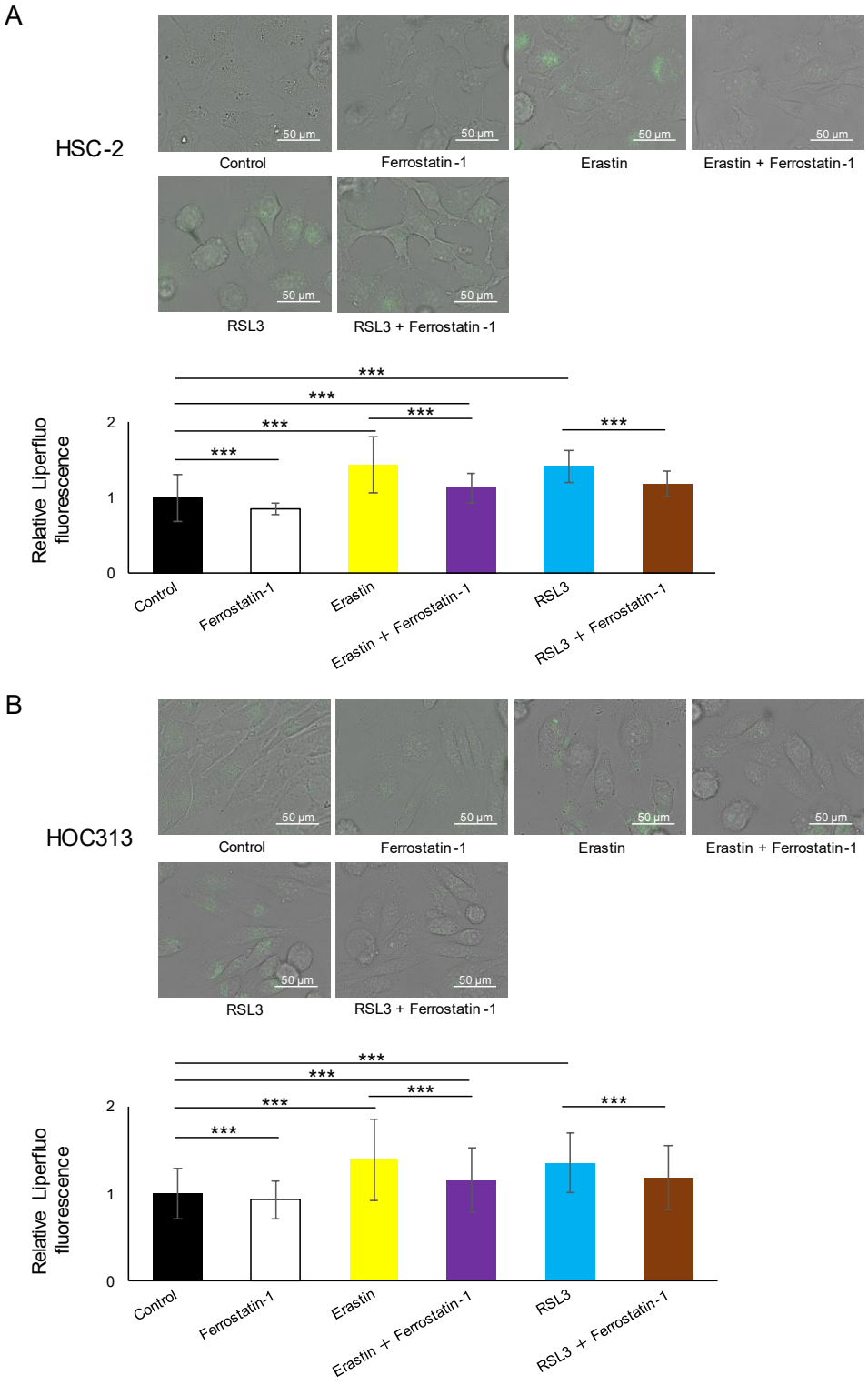

Supplementary Information Figure S2

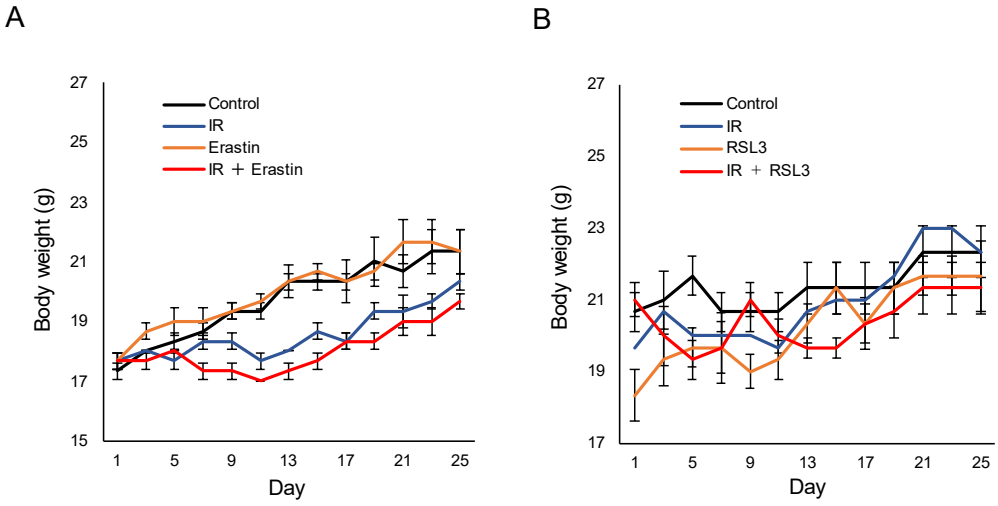

Supplementary Information Table S1

Characteristics	Total	xCT status		*P*-value	GPX4 status		*P*-value	xCT and GPX4 status		*P*-value
		Low n (%)	High n (%)		Low n (%)	High n (%)		Either Low n (%)	Both High n (%)	
	92	58 (63.0)	34 (37.0)		57 (62.0)	35 (38.0)		72 (77.8)	20 (22.2)	
Age, years										
Median	69.5	70.0	69		69	69		69	69	
Range	30-87	39-87	30-87		46-86	30-87		39-87	30-87	
≤ 65	38	22 (57.9)	16 (42.1)	0.511	25 (65.8)	13 (34.2)	0.663	31 (81.6)	7 (18.4)	0.612
> 65	54	36 (66.7)	18 (33.3)		32 (59.3)	22 (40.7)		41 (75.9)	13 (24.1)	
Gender										
Male	55	33 (60.0)	22 (40.0)	0.514	33 (60.0)	22 (40.0)	0.668	42 (76.4)	13 (23.6)	0.797
Female	37	25 (67.6)	12 (32.4)		24 (64.9)	13 (35.1)		30 (81.1)	7 (18.9)	
Primary site										
Tongue	30	21 (70.0)	9 (30.0)	0.020*	10 (33.3)	20 (66.7)	0.852	24 (80.0)	6 (20.0)	0.598
Mandible	24	19 (79.2)	5 (20.8)		15 (62.5)	9 (37.5)		21 (87.5)	3 (12.5)	
Maxilla	18	10 (55.6)	8 (44.4)		10 (55.6)	8 (44.4)		13 (72.2)	5 (27.8)	
Oral floor	10	2 (20.0)	8 (80.0)		7 (70.0)	3 (30.0)		7 (87.5)	3 (12.5)	
Buccal mucosa	10	6 (60.0)	4 (40.0)		5 (50.0)	5 (50.0)		7 (87.5)	3 (12.5)	
pT category										
T2	32	19 (59.4)	13 (40.6)	0.653	21 (65.6)	11 (34.4)	0.657	27 (84.4)	5 (15.6)	0.427
T3, T4	60	39 (65.0)	21 (35.0)		36 (60.0)	24 (40.0)		45 (75.0)	15 (25.0)	
pN category										
N0	51	36 (70.6)	15 (29.4)	0.128	33 (64.7)	18 (35.6)	0.666	44 (86.3)	7 (13.7)	0.045*
N1, N2	41	22 (53.7)	19 (46.3)		24 (58.5)	17 (41.5)		28 (68.3)	13 (31.7)	
Clinical stage										
II	9	4 (44.4)	5 (55.6)	0.282	6 (66.7)	3 (33.3)	1.000	7 (77.8)	2 (22.2)	1.000
III, IV	83	54 (65.1)	29 (34.9)		51 (61.4)	32 (38.6)		65 (78.3)	18 (21.7)	
Differentiation										
Well	76	47 (61.8)	29 (38.2)	0.777	45 (59.2)	31 (40.8)	0.273	60 (78.9)	16 (21.1)	0.744
Moderate	16	11 (68.8)	5 (31.2)		12 (75.0)	4 (25.0)		12 (75.0)	4 (25.0)	
Mode of invasion										
Grade I, II, III	74	49 (66.2)	25 (33.8)	0.276	46 (62.2)	28 (37.8)	1.000	60 (81.1)	14 (18.9)	0.209
Grade IV	18	9 (50.0)	9 (50.0)		11 (61.1)	7 (38.9)		12 (66.7)	6 (33.3)	
Pathological response										
Grade 0, I, IIa, IIb	39	21 (53.8)	18 (46.2)	0.132	22 (56.4)	17 (43.6)	0.390	26 (64.3)	13 (35.7)	0.039*
Grade III, IV	53	37 (69.8)	16 (30.2)		35 (66.0)	18 (34.0)		40 (80.8)	7 (19.2)	